Microwave and infrared spectra of CO–(pH2)2, CO–(oD2)2, and mixed CO–pH2–He trimers

ARTICLE *in* THEORETICAL CHEMISTRY ACCOUNTS · SEPTEMBER 2014

Impact Factor: 2.23

1 AUTHOR:

Hui Li
Jilin University
43 PUBLICATIONS **371** CITATIONS

SEE PROFILE

Theor Chem Acc (2014) 133:1568
DOI 10.1007/s00214-014-1568-4

REGULAR ARTICLE

Microwave and infrared spectra of CO–$(pH_2)_2$, CO–$(oD_2)_2$, and mixed CO–pH_2–He trimers

Xiao-Long Zhang · Hui Li · Robert J. Le Roy · Pierre-Nicholas Roy

Received: 31 May 2014 / Accepted: 19 August 2014

Abstract The microwave and infrared spectra of CO–$(pH_2)_2$, CO–$(oD_2)_2$, and CO–pH_2–He trimers are predicted by performing exact bound state calculations on the global potential energy surfaces defined as the sum of accurately known two-body pH_2–CO or oD_2–CO (in Li et al. J Chem Phys 139:164315, 2013), pH_2–pH_2 or oD_2–oD_2 (in Patkowski et al. J Chem Phys 129:094304, 2008), and pH_2–He pair potentials. A total of four transitions have been reported to date, three in the infrared region, and one in the microwave region, which are in good agreement with our theoretical predictions. Based on selection rules, new transitions for $J \leq 3$ have been predicted, and the corresponding transition intensities at different temperatures are also calculated. These predictions will serve as a guide for new experiments. The weak and tentatively assigned transitions are verified by our calculations. Three-body effects and the quality of the potential are discussed. A reduced-dimension treatment of the pH_2 or oD_2 rotation has been employed by applying the hindered-rotor averaging technique of Li et al. (J Chem Phys 133:104305, 2010). A technique for displaying the three-dimensional pH_2 or oD_2 density in the body-fixed frame is used and shows that in the ground state, the two pH_2 or two oD_2 molecules are localized, while the He's are delocalized.

Keywords Microwave spectra · Infrared spectra · CO–$(pH_2)_2$ trimers · CO–$(oD_2)_2$ trimers · CO–pH_2–He trimers · Reduced-dimension treatment · Exact bound state calculations · Three-body effects

Dedicated to Professor Guosen Yan and published as part of the special collection of articles celebrating his 85th birthday.

Electronic supplementary material The online version of this article (doi:10.1007/s00214-014-1568-4) contains supplementary material, which is available to authorized users.

X.-L. Zhang · H. Li (✉)
Institute of Theoretical Chemistry, State Key Laboratory of Theoretical and Computational Chemistry, Jilin University, 2519 Jiefang Road, Changchun 130023, People's Republic of China
e-mail: Prof_huili@jlu.edu.cn

H. Li · R. J. Le Roy · P.-N. Roy
Department of Chemistry, University of Waterloo, Waterloo, ON N2L 3G1, Canada
e-mail: leroy@uwaterloo.ca

P.-N. Roy
e-mail: pnroy@uwaterloo.ca

1 Introduction

At a very low temperature (<2 K), high-resolution infrared or microwave spectra of a single chromophore molecule doped in helium droplets or clusters have provided a unique opportunity to study quantum solvation and microscopic superfluidity [1–20]. Para-hydrogen (pH_2) or ortho-deuterium (oD_2), like ^{4}He atoms, are bosons. Similarly, a chromophore molecule embedded in pH_2 or oD_2 clusters can also be considered as a possible route to investigate quantum solvation and the superfluidity of pH_2 or oD_2 [21–30]. Recently, combining experimental measurements and theoretical simulations, superfluid response for pH_2 to dopant rotation has been first elucidated in CO2–$(pH_2)_N$ clusters [26]. However, due to localization effects, the superfluid fraction of larger doped hydrogen clusters becomes suppressed. Carbon monoxide (CO) is a gentler probe molecule with much weaker and less anisotropic interaction with pH_2 and a relatively large rotational constant. These features lead to a delocalized distribution of pH_2 molecules with respect to CO. Persistent molecular

Published online: 06 September 2014

superfluid response to dopant rotation in CO–$(pH_2)_N$ clusters has been observed, and this conclusion is supported by both microwave spectroscopy and the theoretical analysis [31].

An understanding of the experimental spectra at the microscopic scale requires complementary computer simulation studies based on accurate intermolecular potential energy functions. Very recently, two reliable ab initio analytical potential energy surfaces (PESs) for H_2–CO dimer have been reported, referred to hereafter V_{12} [32, 33] and V_{MLRQ} [34], respectively. Both PESs explicitly account for the intra-molecular C–O stretch coordinate and allow to describe the infrared spectrum in the region of the fundamental stretching vibration of C–O around 2,143.2712 cm^{-1}. The predicted infrared spectra calculated from these two PESs have already been shown to agree extremely well with the experimental spectra of the pH_2– and oH_2–CO dimers [32–34]. Studies of CO–$(pH_2)_2$ trimer are important for testing the accuracy of pair-wise additive approach by sum of two-body potentials to simulate systems with tens of pH_2 molecules, looking for three-body effects, and for testing the validity of quantum Monte Carlo methods for molecular clusters, since comparisons with exact quantum results are possible.

Although a large number of infrared and microwave transitions were recorded and assigned for CO–He and CO–pH_2 dimers [33, 35–37], only a few transitions for CO–$(pH_2)_2$, CO–$(oD_2)_2$, and CO–pH_2–He trimers were reported, and some weak or tentatively assigned transitions remain to be verified or reassigned [22, 31]. Therefore, reliable theoretical predictions based on exact quantum calculations will provide valuable guidance in confirming or reassigning the measured infrared spectra. Previous work on exact quantum calculations of infrared and microwave spectra for trimer complexes containing one CO, CO_2, N_2O, and OCS molecule attached to two He atoms have been reported, by Wang and Carrington [38–41] and by Li et al. [42], which yield excellent agreement with experiment observations. Exact rovibrational spectra calculations for the trimer containing a single chromophore molecule doped with two pH_2 molecules, such as CO_2–$(pH_2)_2$, were first reported by Li et al. [27] by applying the hindered-rotor averaging technique to treat pH_2 as a point-like particle and consequently reduce the dimension of the potential enemy surface. To date, however, exact quantum calculations for the trimer containing a chromophore molecule doped with two oD_2 or with mixed pH_2 and He have not been reported. Further more, exact quantum calculations for CO–$(pH_2)_N$ clusters have only been limited to CO–pH_2 dimer. In the present paper, we extend such exact quantum calculations to the cases of two pH_2, or two oD_2, or mixed pH_2 and He, attached to one CO dopant molecule. The results are used to help assign or confirm the experimental spectra of CO–$(pH_2)_2$, CO–$(oD_2)_2$, and CO–pH_2–He.

2 Computational methods

2.1 Geometry and reduced-dimension treatment

There are six atoms in CO–$(pH_2)_2$ system, and it takes a 12-dimensional (12D) PES to describe the interaction within the system. If we treat linear CO and the two H_2 as rigid molecules, taking only the intermolecular coordinates into consideration, there are still nine intermolecular degrees of freedom. The geometry of this complex in which CO is rigidly linear, and can be described naturally using the Jacobi coordinates (q_1, q_2, ϑ_1, ϑ_2, ϑ_3, ϑ_4, φ, φ_1, φ_2) is shown on the left panel of Fig. 1, where q_1 and q_2 are the distances from the center of mass of CO to the centers of mass of the two H_2 molecules, ϑ_1 and ϑ_2 are the angles between $\mathbf{q_1}$ or $\mathbf{q_2}$ and a vector pointing from atom O to atom C, ϑ_3 and ϑ_4 are the angles between $\mathbf{q_1}$ and a vector pointing from atom H_2 to atom H_1, and from $\mathbf{q_2}$ to a vector pointing from atom H_4 to atom H_3, φ is the dihedral angle between two planes defined by vector $\mathbf{q_1}$ and $\mathbf{q_2}$ with the

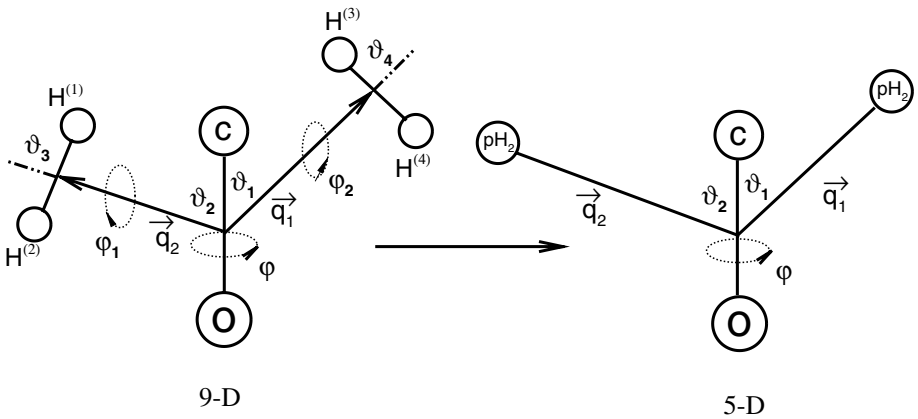

Fig. 1 Jacobi coordinates for the CO–$(H_2)_2$ complex: left side, the geometry describe with nine dimensions of intermolecular coordinates; right side, the geometry described with five dimensions of intermolecular coordinates and with the two para-hydrogen treated as spherical particles

axis of the CO molecule, φ_1 and φ_2 are the azimuthal angles for rotation of H_1–H_2 and H_3–H_4 about vectors $\mathbf{q_1}$ or $\mathbf{q_2}$, respectively.

It is still difficult to solve the nine-dimensional intermolecular Schrodinger equation. However, because the nuclear spins are anti-parallel for para-hydrogen, the rotational angular momentum, J, must be even. We know that the ground-state rotational wave function of an isolated ground-state ($J = 0$) H_2 molecule is precisely spherically symmetric, and the energy spacing to its first-excited ($J = 2$) level is relatively large (354.3735 cm^{-1}). It is therefore desirable to treat pH_2 as a spherical particle. Following this approximation, the nine-dimensional intermolecular coordinates for a CO–$(pH_2)_2$ complex can be reduced to five coordinates (q_1, q_2, ϑ_1, ϑ_2, φ) shown on the right panel of Fig. 1, greatly reducing the computational effort. However, it should be noted that pH_2 is not truly spherical when interacting with other species. A simple spherical average over the orientations of the H_2 moiety does not provide an accurate description [43].

The rotational constant for pH_2(59.322 cm^{-1}) is more than 31 times larger than that of CO in its ground (1.9225288 cm^{-1}) or excited state (1.9050256 cm^{-1}) [44]. It therefore seems reasonable to perform a Born–Oppenheimer-type separation of the fast rotational motion of pH_2 from the relative slower CO rotation. Recently, Li, Roy, and Le Roy introduced a much better reduced-dimension description which they call an "adiabatic-hindered-rotor (AHR)" method. This approximation yields an effective pH_2-{linear molecule} interactions that are an order of magnitude more accurate than those obtained using a simple spherical-average approximation. We expect that with such an AHR approximation, the CO–$(pH_2)_2$ trimer can be accurately described with the left over five degrees of freedom shown in the right panel of Fig. 1. Based on our previous tests for CO–oD_2 dimer, as shown in Table 2 of Ref. [43], we found the AHR treatment of oD_2 is still feasible and reliable, and the differences between {2D–4D} are smaller than 0.092 cm^{-1} for vibrational levels, which are about six times better than those obtained by spherical treatment. Therefore, similar treatment has been applied for the other two trimers of CO–$(oD_2)_2$ and CO–pH_2–He.

The rovibrational energy levels of CO–$(pH_2)_2$, CO–$(oD_2)_2$, and CO–pH_2–He were calculated using the radial discrete variable representation (DVR) and parity-adapted angular finite basis representation (FBR) methods described in Section II. The potential we used for each trimer is a sum of three pair potentials. The CO–pH_2, CO–oD_2, and oD_2–oD_2 potentials were generated by an "adiabatic-hindered-rotor" average treatment of the H_2 or D_2 rotation using dimer potentials taken from Refs. [32, 34, 45], while pH_2–pH_2 potentials were generated by a "spherical" average treatment of the H_2 rotation using dimer potential taken from Ref. [45]. For CO–pH_2–He and CO–$(He)_2$ complexes, the CO–pH_2, CO–He, and He–He potentials of Refs. [34, 46, 47] were used. The rotational constants B_{CO} required for these calculations were fixed at the experimental values of 1.9225288 and 1.9050256 cm^{-1} for CO in their ground ($\upsilon_3 = 0$) and excited ($\upsilon_3 = 1$) states [44], respectively. In our calculations, the masses were set at 1.00782503207 u for H, 2.0141017778 u for D, 4.00260324 u for ^{4}He, 15.994914635 u for ^{16}O, and 12. u for ^{12}C. An 40-point sine DVR grid range from 3.0 to 30.0 bohr was used for the radial r_1 or r_2 stretching coordinate. For the angular basis, we use $l_{max} = m_{max} = 25$; 30 Gauss–Legendre quadrature points were used for the integration over θ_1 or θ_2, while 64 equally spaced points in the range [0, 2π] were used for the integration over ϕ. It is useful to apply a potential ceiling value to reduce the spectral range and accelerate the convergence of the Lanczos calculation [48]. In our calculations, we use a ceiling of 1,000 cm^{-1} and have confirmed that low-lying energy levels change by less than 0.001 cm^{-1} when the ceiling is raised to 10,000 cm^{-1}.

2.2 Hamiltonian and basis functions

Following our previous work for CO_2–$(pH_2)_2$ trimer [27], in Radau coordinate, we use the Hamiltonian and basis functions based mainly on the work of Wang et al. [39] and on fundamental ideas presented by Mladenovic [49]. In recent years, this approach have been successfully used to treat N_2O–$(He)_2$, CO–$(He)_2$, CO_2–$(He)_2$, OCS–$(He)_2$, and CO_2–$(pH_2)_2$ complexes. The method is briefly reviewed here, and the reader is referred to Refs. [39] and [27] for further details. With the AHR approximation, the rovibrational Hamiltonian of the CO–$(pH_2)_2$ complex in the CO molecule-fixed frame has the form (in a.u.) [39, 49–51],

$$\hat{H} = \hat{T}_{str} + \hat{T}_{diag} + \hat{T}_{off} + \hat{T}_{Cor} + \bar{V}(r_1, r_2, \theta_1, \theta_2, \phi) \tag{1}$$

in which

$$\hat{T}_{str} = -\frac{1}{2m_{H_2}}\frac{\partial^2}{\partial r_1^2} - \frac{1}{2m_{H_2}}\frac{\partial^2}{\partial r_2^2} \tag{2}$$

$$\begin{aligned}\hat{T}_{diag} = &-\left(\frac{1}{2m_{H_2}r_1^2} + B_{CO}\right)\left[\frac{\partial^2}{\partial\theta_1^2} + \cot\theta_1\frac{\partial}{\partial\theta_1} - \frac{1}{\sin^2\theta_1}(\hat{J}_z - \hat{l}_{2z})^2\right] \\ &+ \left(\frac{1}{2m_{H_2}r_2^2} + B_{CO}\right)\hat{l}_2^2 + B_{CO}[\hat{J}^2 - 2(\hat{J}_z - \hat{l}_{2z})^2 - 2\hat{J}_z\hat{l}_{2z}]\end{aligned} \tag{3}$$

$$\hat{T}_{off} = B_{CO}[\hat{l}_{2+}\hat{a}_1^- + \hat{l}_{2-}\hat{a}_1^+] \tag{4}$$

$$\hat{T}_{Cor} = -B_{CO}[\hat{J}_-\hat{a}_1^+ + \hat{J}_+\hat{a}_1^- + \hat{J}_-\hat{l}_{2+} + \hat{J}_+\hat{l}_{2-}] \tag{5}$$

where

$$\hat{J}_{\pm} = \hat{J}_x \pm i\hat{J}_y, \quad \hat{l}_{2\pm} = \hat{l}_{2x} \pm i\hat{l}_{2y} \tag{6}$$

$$\hat{a}_1^{\pm} = \pm\frac{\partial}{\partial\theta_1} - \cot\theta_1(\hat{J}_z - \hat{l}_{2z}) \tag{7}$$

The details of the coordinate system are shown in Fig. 2. r_1 and r_2 are the lengths of Radau (or orthogonalized satellite) vectors $\mathbf{r_1}$ and $\mathbf{r_2}$, which are linear combinations of the Jacobi vectors $\mathbf{q_1}$ and $\mathbf{q_2}$ running from the center of mass of CO to the centers of the pH_2 molecules [49]. The polyspherical angles (θ_1, θ_2, ϕ) are determined by the three vectors ($\mathbf{r_0}$, $\mathbf{r_1}$, $\mathbf{r_2}$). θ_1 is the angle between the dopant axis $\mathbf{r_0}$ and $\mathbf{r_1}$, θ_2 and ϕ are the polar angles that specify the orientation of $\mathbf{r_2}$ with respect to the CO molecule-fixed frame. m_{H2} is the mass of the pH_2 molecule and B_{CO} is the rotation constant of CO. The operators $\mathbf{J_x}$, $\mathbf{J_y}$, and $\mathbf{J_z}$ are the components of the total angular momentum operator $\mathbf{J}$ in the body-fixed frame, the z axis of the body-fixed frame lies along the Jacobi radial vector $\mathbf{r_0}$, and the x axis is in the plane that contains $\mathbf{r_0}$ and one pH_2 molecule. Here, $\overline{V}(r_1, r_2, \theta_1, \theta_2, \phi)$ is the total potential energy function which is represented as a sum of two two-dimensional AHR pH_2–CO potentials [34, 43] plus the one-dimensional AHR pH_2–pH_2 intermolecular potential [45]. The above Hamiltonian contains full vibration–rotation coupling.

A sine DVR grid [52] is used for the r_1 and r_2 degrees of freedom, while parity-adapted rovibrational basis functions are used for the angular part. A complete product basis function is

$$u^{J,M,P}_{l_1,l_2,m_2,K} = \frac{1}{\sqrt{2(1+\delta_{m_2,0}\delta_{K,0})}}[|l_1, l_2, m_2, K; J, M\rangle + (-1)^{J+P}|l_1, l_2, -m_2, -K; J, M\rangle] \tag{8}$$

where $K > 0$, and $P = 0$ and 1 correspond to even and odd parities, respectively. If $K = 0$, then it is necessary to apply the constraint $m_2 \geq 0$ to get rid of the redundant basis. The combination $m_2 = K = 0$ and $(-1)^{J+P} = -1$ is not allowed. The parity-adapted basis makes it possible to calculate even and odd parity levels separately. Within each parity block, we use the symmetry-adapted Lanczos algorithm (SAL) [53, 54] to compute states that are symmetric (A) and antisymmetric (B) with respect to exchange of the two pH_2 or oD_2 in trimers of CO–$(pH_2)_2$ or CO–$(oD_2)_2$, while no exchange symmetry applied for CO–pH_2–He Trimer.

3 Results and discussion

3.1 Features of the five-dimensional potential energy surface

Figure 3 shows how the well depth of our vibrationally averaged five-dimensional V_{MLRQ} ground-state PES for

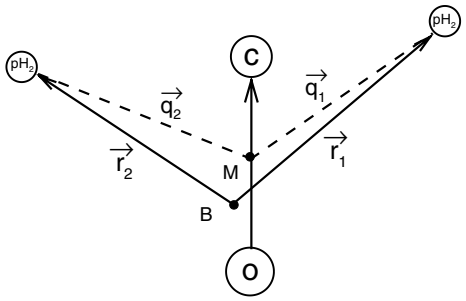

Fig. 2 M is the center of mass of CO, and B is the canonical point for the Radau vectors. $\mathbf{q_1}$ and $\mathbf{q_2}$ are Jacobi vectors. $\mathbf{r_1}$ and $\mathbf{r_2}$ are Radau vectors. ϕ is a dihedral angle between $\mathbf{r_1}$ and $\mathbf{r_2}$ around $\mathbf{r_0}$. $\theta_1(\theta_2)$ are angles between $\mathbf{r_0}$ and $\mathbf{r_1}(\mathbf{r_2})$

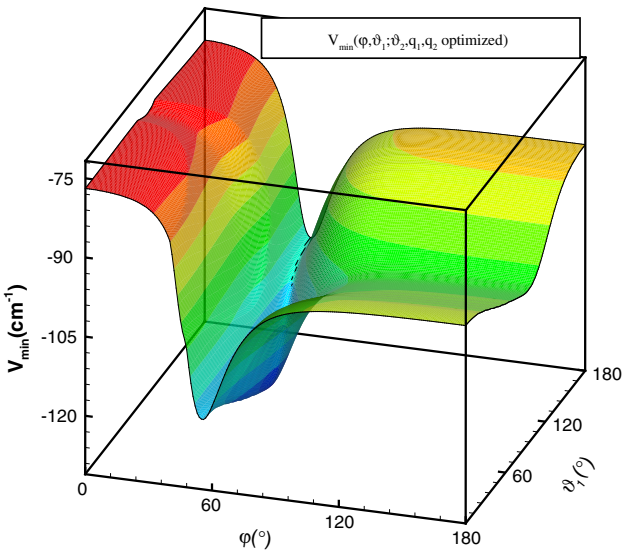

Fig. 3 Minimum energy on our vibrationally averaged five-dimensional PES for CO($\upsilon = 0$)–$(pH_2)_2$ trimer as a function of angles φ and ϑ_1, for optimized values of ϑ_2, q_1, and q_2

CO($\upsilon = 0$)–$(pH_2)_2$ system depends on φ and ϑ_1, when ϑ_2, q_1, q_2 are optimized to minimize the energy for each (φ, ϑ_1). As seen there, the global minima with well depth of -126.06 cm^{-1} occur at the geometries ($\vartheta_1 = 95.6°$, $\vartheta_2 = 95.6°$) with $q_1 = q_2 = 3.57$ Å and $\varphi = 58.0°$ (or by symmetry of $\varphi = 302.0°$). Between these two identical global minima, there exists a saddle point with energy -101.90 cm^{-1} located at $\vartheta_1 = \vartheta_2 = 95.3°$ with $q_1 = q_2 = 3.57$ Å and $\varphi = 180.0°$, which corresponds to a coplanar geometry with the two pH_2 molecules on opposites of the CO molecule. In addition, Fig. 3 also shows local minimum with energy of -77.59 cm^{-1} occurs at the coplanar geometry ($\vartheta_1 = 94.7°$, $\vartheta_2 = 180.0°$) with $q_1 = 3.56$ Å, $q_2 = 7.01$ Å, and $\varphi = 0.0°$. Parameters characterizing the various stationary configurations and energies for the CO–$(pH_2)_2$ trimer are summarized in Table 1, where

Table 1 Properties of stationary points of the CO($\upsilon = 0$)–$(pH_2)_2$ potential energy surface, and comparisons with those results for CO($\upsilon = 0$)–$(oD_2)_2$ and CO($\upsilon = 0$)–$(He)_2$ surfaces

	Global minimum	Saddle point	Local minimum
CO–$(pH_{2)2}(V_{MLRQ})$	{3.57, 3.57, 95.6, 95.6, 58.0, −126.06}	{3.57, 3.57, 95.3, 95.3, 180.0, −101.90}	{3.56, 7.01, 94.7, 180.0, 0.0, −77.59}
CO–$(pH_2)_2(V_{12})$	{3.57, 3.57, 94.7, 94.7, 58.0, −126.22}	{3.57, 3.57, 94.7, 94.7, 180.0, −102.07}	{3.56, 7.01, 94.0, 180.0, 0.0, −77.74}
CO–$(oD_2)_2(V_{MLRQ})$	{3.57, 3.57, 95.2, 95.2, 58.0, −126.91}	{3.56, 3.56, 94.6, 94.6, 180.0, −102.76}	{3.56, 7.01, 96.0, 180.0, 0.0, −78.07}
CO–$(He)_2(V_{MLRQ})$	{3.39, 3.39, 120.8, 120.8, 51.9, −53.47}	{3.39, 3.39, 120.8, 120.8, 180.0, −45.90}	{3.37, 6.31, 118.3, 0.0, 0.0, −32.22}

All entries are given as $\{q_1[\text{Å}], q_2[\text{Å}], \vartheta_1^\circ, \vartheta_2^\circ, \varphi^\circ, \Delta V[\text{cm}^{-1}]\}$

they are consistent with corresponding values obtained on V_{12} PES, and compared with properties of the analogous CO–$(oD_2)_2$ and CO–$(He)_2$ species. As shown in Table 1, all the stationary points (the global minimum, saddle point, and local minimum) for CO–$(pH_2)_2$ are more than twice as deep as those of CO–$(He)_2$. This will be mostly due to the polarizability of pH_2 (5.414 au) [55] is four times larger than that for He (1.383 au) [56]. Comparing CO–$(pH_2)_2$ and CO–$(oD_2)_2$ yields the differences at the global minimum, saddle point, and local minimum are 0.85, 0.86, and 0.48 cm^{-1}, respectively. Those differences originate from the fact that $B_{D2}/B_{H2} \approx 0.5$, which means the solution of the two-dimensional angular rotational equation for oD_2 systems will have substantially larger contributions from basis functions corresponding to $L > 0$ [43], where L is the angular momentum quantum number of H_2 rotation. Figure 4 shows the minimum energy paths between equivalent global minima as a function of φ, for optimized values of ϑ_1, ϑ_2, q_1 and q_2.

As clearly shown in Fig. 4(b), the comparison between CO–$(pH_2)_2$ and CO–$(He)_2$ shows that the anisotropy with respect to the dihedral torsional motion of the two pH_2 molecules in CO–$(pH_2)_2$ (48.47 cm^{-1}) is more than twice as strong as that for the analogous motion in the CO–$(He)_2$ (21.25 cm^{-1}) complex. It also shows that the barrier between two adjacent minima of CO–$(pH_2)_2$ (24.16 cm^{-1}) is more than three times higher than that for CO–$(He)_2$ (7.57 cm^{-1}). As would be expected, these barrier heights are approximately equal to the well depths for pH_2–pH_2 (24.71 cm^{-1}) [45] and He–He (7.65 cm^{-1}) [47] dimers, respectively. These differences in PESs will still be reflected in the different spectra of the Trimers.

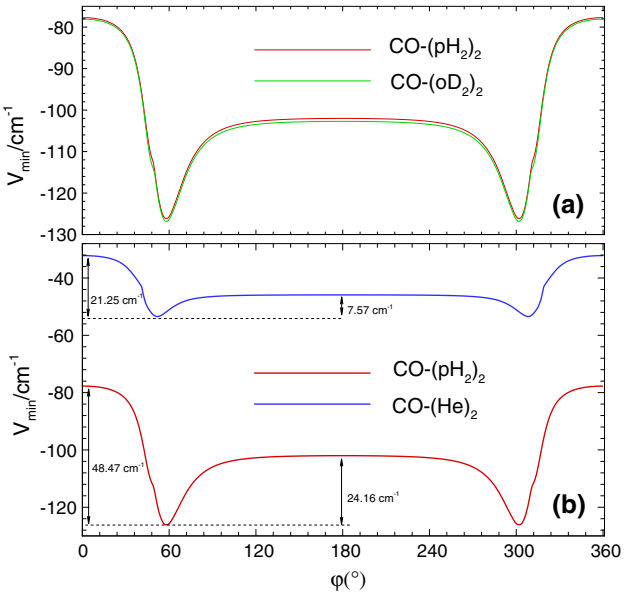

Fig. 4 Minimum energy path on our vibrationally averaged five-dimensional PES for CO($\upsilon = 0$)–$(pH_2)_2$ trimer as functions of angle φ for optimized values of ϑ_1, ϑ_2, and q_1, q_2

3.2 Rovibrational energy levels and band origin shifts

The calculated intermolecular rovibrational energy levels for the ground ($\upsilon = 0$) states of CO–$(pH_2)_2$, CO–$(oD_2)_2$, and CO–pH_2–He trimers with $J = 0$, 1, 2, and 3 are listed in Table 2, which are relative to the corresponding zero point energies of −42.907, −59.326, and −26.671 cm^{-1}, respectively. Those for excited ($\upsilon = 1$) (not shown here) are very similar and listed in Table S1 of the supplementary material. The rovibrational energy levels are labeled by quantum numbers (J, P, $n_{J,P}$). The only good quantum numbers are the overall angular momentum J and parity P = e or f. The label $n_{J,P}$ numbers consecutive states for each (J,P). As shown in Table 2, symmetry (A) and antisymmetry (B) are used to label the symmetries with respect to permutation of the two pH_2 or oD_2 molecules, (A, e) and (B, e) for even parity and (A, f) and (B, f) for odd parity. Because of the zero nuclear spin of the ^{4}He, pH_2, oD_2, therefore for CO–$(pH_2)_2$, CO–$(He)_2$ and CO–$(oD_2)_2$ trimers, only (A, e) and (A, f) states are physically allowed. However, for CO–pH_2–He trimer, without exchange symmetry between pH_2 and He, only even and odd parity blocks are used to sort the rovibrational energy levels.

In order to assign the torsional motion states for CO–$(pH_2)_2$ trimer, it is very useful to yield a one-dimensional representation of the partial wave functions along the

Table 2 Calculated $J = 0$, 1, 2, 3 rovibrational energy levels (in cm^{-1}) for CO($\upsilon = 0$)–(pH_2)$_2$, CO($\upsilon = 0$)–(oD_2)$_2$, and CO($\upsilon = 0$)–pH_2–He complexes, which are relative to the corresponding zero point energies of −42.907, −59.326, and −26.671 cm^{-1}, respectively

CO($\upsilon = 0$)–(pH_2)$_2$				CO($\upsilon = 0$)–(oD_2)$_2$				CO($\upsilon = 0$)–pH_2–He	
(A,e)	(B,e)	(A,f)	(B,f)	(A,e)	(B,e)	(A,f)	(B,f)	e	f
$J = 0$									
0.000 (0)	5.477	14.782	3.407 (1)	0.000 (0)	4.852	12.839	2.728 (1)	0.000 (0)	4.065 (1)
5.340 (2)	12.753	22.294	10.947 (3)	7.299 (2)	13.559	22.401	11.516 (3)	2.580 (2)	8.378 (3)
6.951	14.491	24.140	14.932	7.915	15.141	23.522	14.116	4.991	11.280
11.901 (4)	18.603	27.663	19.647 (5)	11.140 (4)	18.436	27.299	16.553 (5)	6.651	11.407
$J = 1$									
3.597	1.352	0.736	1.136	3.001	0.773	0.399	0.692	1.197	0.517
7.662	3.943	3.438	5.973	6.038	3.103	3.005	5.219	4.058	0.985
11.532	7.972	7.398	6.078	11.856	8.093	5.977	7.956	4.362	3.091
14.271	8.708	7.745	8.125	13.123	9.437	7.752	8.283	5.354	3.897
$J = 2$									
2.083	2.426	4.126	2.945	1.181	1.410	2.508	1.650	1.494	2.319
4.074	4.758	4.865	4.857	2.521	3.910	3.740	3.830	1.778	3.235
4.558	7.337	8.609	5.168	3.754	5.958	6.839	3.941	3.080	4.848
7.307	8.967	9.926	10.283	6.659	8.591	9.742	8.589	4.197	5.198
$J = 3$									
6.326	5.199	4.022	4.234	3.707	2.947	2.317	2.476	3.969	2.792
6.776	6.713	6.193	6.436	4.832	4.896	3.770	4.986	4.501	3.097
7.754	6.974	6.443	7.612	5.785	5.104	4.858	5.264	6.028	4.150
10.860	8.148	7.705	9.314	8.049	5.270	5.790	7.075	6.309	5.538

The torsional motion assignments are indicated in parentheses as υ_t

dihedral angle ϕ. In terms of the basis functions and Radau coordinate system, the wavefunction for the n'th energy level for a given set of $\{J, M, P\}$ quantum numbers is,

$$\begin{aligned}\Psi_n^{J,M,P}(r_1, r_2, \theta_1, \theta_2, \phi; \alpha, \beta, \gamma) \\ = \sum_{\alpha_1,\alpha_2,l_1,l_2,m_2,K} \langle \theta_1, \theta_2, \phi; \alpha, \beta, \gamma \mid l_1, l_2, m_2; J, K, M, P \rangle \langle r_1 \mid \alpha_1 \rangle \langle r_2 \mid \alpha_2 \rangle \\ \times \left\langle \alpha_1, \alpha_2, l_1, l_2, m_2; J, K, M, P \,\middle|\, \Psi_n^{J,M,P} \right\rangle,\end{aligned} \tag{9}$$

in which $\langle r_j \mid \alpha_j \rangle$ is a localized DVR basis function for particle j, and the coefficient $\left\langle \alpha_1, \alpha_2, l_1, l_2, m_2; J, K, M, P \,\middle|\, \Psi_n^{J,M,P} \right\rangle$ is an eigenvector obtained via Lanczos diagonalization. The one-dimensional wave function along the dihedral angle ϕ, $\Psi_n^{J,M,P}$ is defined as

$$\begin{aligned}\psi^{J,M,P,n}(\phi) = \int dr_1 dr_2 \sin\theta_1 d\theta_1 \sin\theta_2 d\theta_2 \Psi_n^{J,M,P} \\ \times (r_1, r_2, \theta_1, \theta_2, \phi; \alpha, \beta, \gamma)\end{aligned} \tag{10}$$

The above integral can be evaluated on the same grid as the potential integral. The torsional motion states for CO–(pH_2)$_2$ trimer are assigned and indicated in parentheses as (υ_t) in Table 2, using the partial wave functions, which are yielded by integrating over all degrees of freedom except the dihedral angle ϕ. We make the assignment based on the nodal structure of the partial wave function shown in Fig. 5.

Table 3 presents the calculated zero point energies (ZPEs) and band origin shifts for CO containing dimer or trimer complexes formed from CO(υ) with one or two pH_2, oD_2, He, or mixed one pH_2 and one He. ZPEs are relative to the energies at the dissociation limits for corresponding dimers or trimers. All the band origin shifts are calculated by $\Delta\upsilon_0 = E_{\upsilon=1}^{\mathrm{ZPE}} - E_{\upsilon=0}^{\mathrm{ZPE}}$. As shown in Table 3, the band origin shift for CO–(pH_2)$_2$ trimer predicted by our five-dimensional reduced-dimension V_{MLRQ} PES is −0.369 cm^{-1}, which is almost twice the value of −0.179 cm^{-1} for CO–pH_2 dimer and slightly lower than the estimated experimental value of −0.355 cm^{-1} [31], which was indirectly determined by combining the microwave and the a-type infrared transitions, assuming that the rotational frequencies are the same in the ground and first-excited vibrational states. For CO–(oD_2)$_2$ or CO–(He)$_2$ trimer, the predicted band origin shift of −0.420 or −0.049 cm^{-1}, is approximately equal to twice of −0.206 or −0.024 cm^{-1} for CO–oD_2 or CO–He dimer.

For CO–pH_2–He trimer, two CO–He potentials of CBS + Corr [57] and V333 [46] were used for comparison. The CBS + Corr surface by Peterson and McBane was a three-dimensional ab initio PES that explicitly incorporates dependence on the C–O stretching, obtained with state-of-the-art ab initio and extrapolation methods. The V333 surface [46] by Chuaqui et al. [57] was a two-dimensional PES with CO fixed at its equilibrium geometry, obtained by fitting

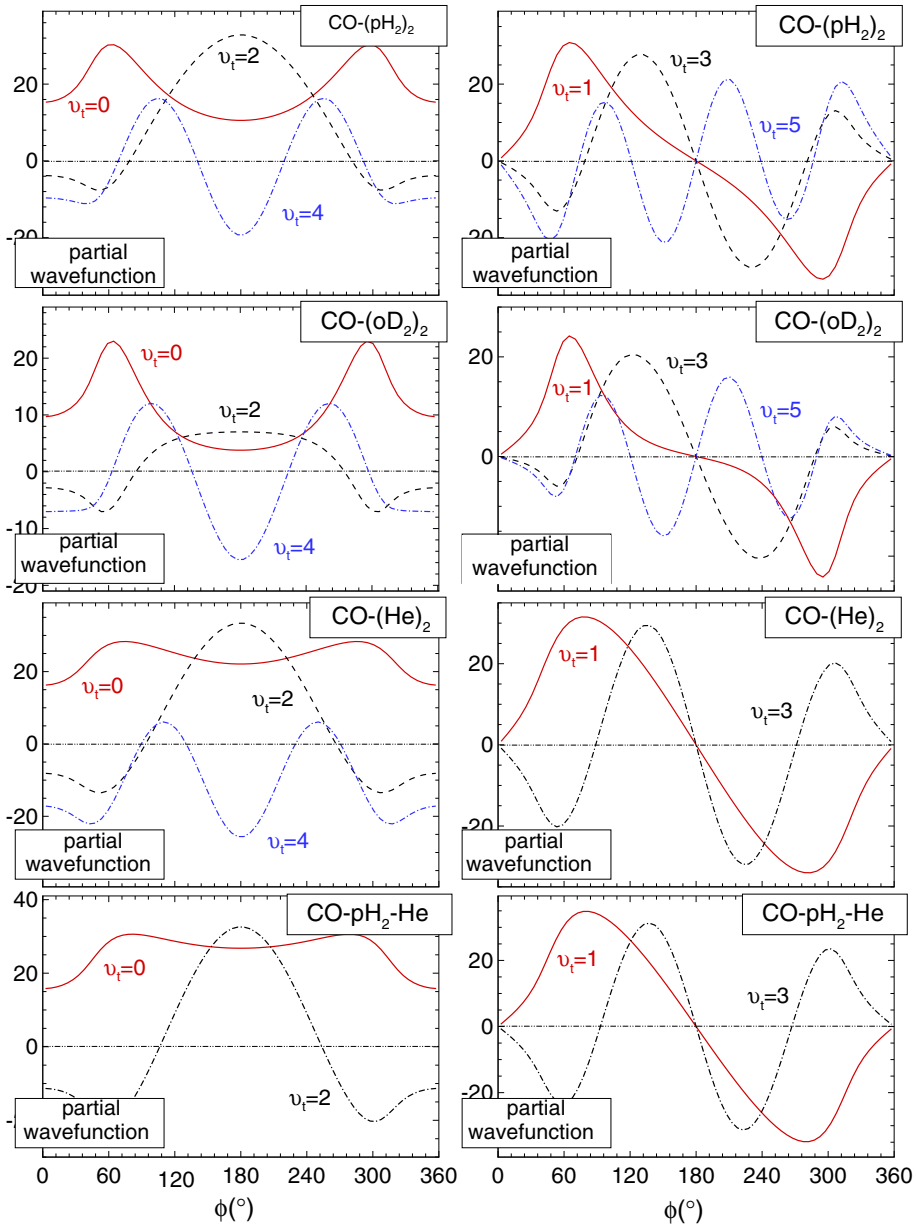

Fig. 5 Partial wave functions for the torsional motion υ_t of CO–$(pH_2)_2$ complex as a function of the azimuthal angle ϕ, compared with those of CO–$(oD_2)_2$, CO–$(He)_2$, CO–pH_2–He complexes

a potential to observed transitions near the fundamental band of CO. As we expected, the calculated band origin shift for CO–pH_2–He trimer is -0.205 cm^{-1} on CBS + Corr potential for CO–He, which is approximately equal to the sum of the band origin shifts of -0.179 and -0.024 cm^{-1} for CO–pH_2 and CO–He dimers, respectively. This indicates that the density for pH_2 or He in CO–pH_2–He trimer has very similar distribution as that in their dimers. Due to V333 potential for CO–He without taking into account the CO vibration, the predicted band origin shift on this surface for CO–pH_2–He trimer is -0.019 cm^{-1} different from that on CBS + Corr potential, which is very close to the calculated shift value of -0.024 cm^{-1} for CO–He dimer.

3.3 Predicted microwave and infrared transitions

For CO–$(pH_2)_2$, the predicted microwave (MW) and infrared (IR) transition frequencies (cm^{-1}) from our AHR 5D V_{MLRQ} potential are listed in Tables 4 and 5, respectively, and compared with those calculated on V_{12} potential and experimental results. The lower and upper states involved in the transitions are numbered with the set of parameters (J, P, $n_{J,P}$). For infrared transitions, to compare our computed energy transitions directly with experimental results, we calculate IR rovibrational transitions from

$$\upsilon = \upsilon_0(\mathrm{CO}) + E^{\mathrm{upper}}_{v=1} - E^{\mathrm{lower}}_{v=0} \tag{11}$$

Table 3 The zero point energies (ZPEs) and band origin shifts for the complexes formed from stretch CO(υ) with one or two pH_2, oD_2, or mixed one pH_2 and one He

Complexes	$E_{v=0}^{ZPE}$	$E_{v=1}^{ZPE}$	$\Delta\upsilon_0$(calc.)	$\Delta\upsilon_0$(obs.)
CO(υ)–pH_2	−19.371	−19.550	−0.179	−0.179[a]
CO(υ)–$(pH_2)_2$	−42.907	−43.276	−0.369	−0.355[b]
CO(υ)–oD_2	−25.630	−25.836	−0.206	−0.202[c]
CO(υ)–$(oD_2)_2$	−59.326	−59.746	−0.420	
CO(υ)–He[f]	−6.431	−6.455	−0.024	−0.025[d]
CO(υ)–$(He)_2$[f]	−13.130	−13.179	−0.049	−0.049[e]
CO(υ)–pH_2–He[g]	−26.671	−26.857	−0.186	
CO(υ)–pH_2–He[f]	−26.459	−26.664	−0.205	

ZPEs are relative to the energies at the dissociation limits for corresponding dimers or trimers. $\Delta\upsilon_0 = E_{\upsilon=1}^{ZPE} - E_{\upsilon=0}^{ZPE}$ is the resulting band origin shifts. All energies are in cm^{-1}

[a] Reference [35]. [b] Reference [31]. [c] Reference [58]

[d] Reference [36]. [e] Reference [38]

[f] This calculation is with the CBS + Corr potential [57]

[g] This calculation is with the V333 potential [46]

where, $\upsilon_0(CO) = 2{,}143.2712\ cm^{-1}$ is the experimental fundamental vibrational transition frequency of a free CO molecule.

As shown in column 2 of Tables 4 or 5, the transition energies yielded by our V_{MLRQ} PES are seen to agree very well with the experimental values shown in column 3 of Tables 4 or 5. The differences seen in column 5 are very small both for microwave and infrared transitions, yielding a root-mean-square (rms) discrepancy of only 0.010 cm^{-1} for all 4 observed transitions (1 for MW and 3 for IR), and also consistent with those obtained on the V_{12} potential as shown in column 5 with the same rms discrepancy for those 4 experimental transitions. To predict more possible microwave and infrared transitions for CO–$(pH_2)_2$ trimer, the line strength and relative intensity at temperatures 0.6 K (effective experimental rotational temperature) are also computed from the wave functions. Note that the line strength does not depend on the temperature. Subject to the selection rules $\Delta J = 0, \pm 1$, $\Delta P = e \leftrightarrow f$, and with line strength larger than $10^{-3}(\mu_{CO}^2)$, 64 possible allowed transitions for MW and 129 for IR with $J \leq 3$ and $n \leq 4$ are predicted. To select most possible microwave and infrared transitions for CO–$(pH_2)_2$ trimer, all the relative intensities at temperature 0.6 K are calculated, and expressed relative to (1, f, 2)−(0, e, 1) transition, whose intensity is set to 1. With the restriction of the relative intensity larger than 10^{-3}, only 15 strongest transitions for MW and 18 for IR are kept and listed in Tables 4 and 5, respectively. The predicted 129 line strengths and 18 relative intensities for CO–$(pH_2)_2$ trimer at temperature of 0.6 K are clearly illustrated in the uppermost segment of Fig. 6.

For CO–$(oD_2)_2$ and CO–pH_2–He, the predicted infrared transition frequencies expressed relative to the band origin 2,143.2712 cm^{-1} of a free CO from our AHR 5D V_{MLRQ} potential are given in Tables 6 and 7, respectively. The lower and upper states involved in the transitions are also numbered with the set of parameters (J, P, $n_{J,P}$). Only the transitions between A+ and A− states are physically allowed for CO–$(oD_2)_2$, but this restriction does not apply to CO–pH_2–He. Subject to overall selection rules $\Delta J = 0$, ± 1, $\Delta P = e \leftrightarrow f$, with line strength larger than 10^{-3} (μ_{CO}^2), $J \leq 3$ and $n \leq 4$, 149 line strengths and 32 most possible allowed IR transitions at temperature of 0.6 K for

Table 4 Predicted microwave frequencies (cm^{-1}), line strengths, and relative intensities at temperature of 0.6 K for CO–$(pH_2)_2$ complex from vibrationally averaged five-dimensional V_{12} or V_{MLRQ} PES, comparison with experimental results

Transitions			Diff. (Calc. − Obs.)		Line	Intensity
Upper–lower	V_{MLRQ}	Obs.	V_{12}	V_{MLRQ}	strength	(0.6 K)
(1, f, 1)–(0, e, 1)	0.736	0.741	0.002	−0.005	0.061	0.047
(2, f, 2)–(2, e, 1)	2.783				1.853	0.010
(1, e, 1)–(1, f, 1)	2.862				0.957	0.126
(1, f, 2)–(0, e, 1)	3.438				1.294	1.000
(2, e, 3)–(1, f, 1)	3.822				0.679	0.090
(3, f, 2)–(2, e, 1)	4.110				0.521	0.003
(1, f, 3)–(2, e, 1)	5.315				0.225	0.001
(3, f, 4)–(2, e, 1)	5.622				0.162	0.001
(0, e, 3)–(1, f, 1)	6.951				0.205	0.158
(2, f, 3)–(2, e, 1)	6.526				0.312	0.002
(1, e, 2)–(1, f, 1)	6.926				0.079	0.011
(1, f, 3)–(0, e, 1)	7.236				0.105	0.082
(1, f, 4)–(0, e, 1)	7.398				0.326	0.252
(2, f, 4)–(2, e, 1)	7.844				0.489	0.003
(1, e, 3)–(1, f, 1)	10.796				0.141	0.019

The lower and upper states involved in the transitions are numbered with the set of parameters (J, P, $n_{J,P}$). The line strength values are multiplied by 100

Table 5 Predicted infrared transition frequencies (cm^{-1}), line strengths, and relative intensities at temperature of 0.6 K for CO–$(pH_2)_2$ complex from vibrationally averaged five-dimensional V_{12} or V_{MLRQ} PES, comparison with experimental results

Transitions			Diff. (calc. − obs.)		Line	Intensity
Upper–lower	V_{MLRQ}	Obs.	V_{12}	V_{MLRQ}	Strength	(0.6 K)
(0, e,1)–(1, f, 1)	2,142.167				0.062	0.008
(1, f, 1)–(0, e, 1)	2,143.638	2,143.657	0.007	0.019	0.001	0.051
(2, e, 1)–(1, f, 1)	2,144.250				0.051	0.007
(2, f, 1)–(2, e, 1)	2,144.945				0.100	0.001
(2, f, 2)–(2, e, 1)	2,145.671				1.848	0.010
(1, e, 1)–(1, f, 1)	2,145.747				0.959	0.127
(1, f, 2)–(0, e, 1)	2,146.324	2,146.330	0.015	0.006	1.293	1.000
(2, e, 3)–(1, f, 1)	2,146.713	2,146.712	0.011	−0.001	0.673	0.089
(3, f, 2)–(2, e, 1)	2,147.586				0.514	0.003
(1, f, 3)–(2, e, 1)	2,148.201				0.224	0.001
(3, f, 4)–(2, e, 1)	2,148:893				0:161	0.001
(0, e, 3)–(1, f, 1)	2,149.108				0.204	0.027
(2, f, 3)–(2, e, 1)	2,149.414				0.311	0.002
(1, e, 2)–(1, f, 1)	2,149.809				0.079	0.010
(1, f, 3)–(0, e, 1)	2,150.283				0.103	0.079
(1, f, 4)–(0, e, 1)	2,150.637				0.330	0.256
(2, f, 4)–(2, e, 1)	2,150.733				0.498	0.003
(1, e, 3)–(1, f, 1)	2,153.693				0.141	0.019

The lower and upper states involved in the transitions are numbered with the set of parameters (J, P, $n_{J,P}$). The line strength values are multiplied by 10

CO–$(oD_2)_2$, and 118 line strengths and 37 most possible IR transitions for CO–pH_2–He are predicted, and shown in the middle and lowermost segments of Fig. 6, respectively. Although MW or IR transitions for CO–$(oD_2)_2$ have not been reported yet, one transition marked "m" in Fig. 7 of Ref. [22] was tentatively assigned as b-type $R(0)$ of the mixed ternary cluster CO–pH_2–He. Based on the calculated line position and intensity, this line may correspond to the (1, f, 4)–(0, e, 1) transition. We are confident for this assignment, not only because the calculated transition at 2,146.958 cm^{-1} are in good agreement with the experimental position at 2,146.93 cm^{-1}, but also the relative intensity for (1, f, 4)–(0, e, 1) at temperature 0.6 K is the strongest among all predicted transitions for CO–pH_2–He complex.

3.4 The wave functions and "solvent" density distributions

Examining the wave function of some of the vibrational states with $\upsilon = 0$ and $J = 0$ helps us to understand the nature about the motions of the pH_2, oD_2, and He in their complexes. We are most interested in the ϕ dependence of the wave function because this coordinate plays an important role in assigning and understanding many vibrational states. Figure 5 shows the reduced wave functions with (A,e) symmetry and (B,f) symmetry for $\upsilon_t = 0$, 1, 2, 3, 4, and 5 levels of CO–$(pH_2)_2$, obtained by integrating the wave function over the coordinates of r_1, r_2, θ_1 and θ_2 at each value of ϕ, and compared with those of CO–$(oD_2)_2$, CO–$(He)_2$, and CO–pH_2–He trimers. As shown in Fig. 5, the wave functions for the $\upsilon_t = 1$, 3, and 5 levels shown on the right side have strikingly regular nodal structures along the ϕ coordinate with exact zero at $\phi = 0$ or $\phi = 180°$, which implies that there is little coupling between ϕ with the other coordinates. While the wave functions for $\upsilon_t = 0$, 2, and 4 levels shown on the left side have no strict characteristics as torsional states, which is probably due to the fact that there is strong coupling between ϕ with the other coordinates that distort their character. For CO–$(He)_2$ and CO–pH_2–He trimers, there exist strong coupling between many (A,e) or (A,f) states, and it is hard to assign those states as torsional motions; thus, we only presented the lowest possible torsion states with $\upsilon_t < 4$. In Fig. 5, it can be clearly seen that the wave functions for the $\upsilon_t = 0$, 2, and 4 levels are quite different between the CO–$(pH_2)_2$ and CO–$(He)_2$ complexes, but very similar for CO–$(pH_2)_2$ and CO–$(oD_2)_2$, and for CO–$(He)_2$ and CO–pH_2–He complexes. In particular, for the $\upsilon_t = 0$ and 1 levels, the highly localized distribution for pH_2 or oD_2 in CO–$(pH_2)_2$ or CO–$(oD_2)_2$ complexes contrasts sharply with that for He in CO–$(He)_2$ or CO–pH_2–He complexes. In addition to the expected excluded volumes near $\phi = 0$ and $\phi = 360$, for the ground state of CO–$(pH_2)_2$ or CO–$(oD_2)_2$, there are local maxima at $\phi = 58$ and $\phi = 302°$ corresponding to the pH_2 or oD_2 particles lying at global minimum positions, while the He distribution in CO–$(He)_2$ or CO–pH_2–He is delocalized, even with a lot of distribution at $\phi = 180°$.

Figure 7 shows the three-dimensional density for the two pH_2 molecules (upper), two He atoms (middle), or mixed

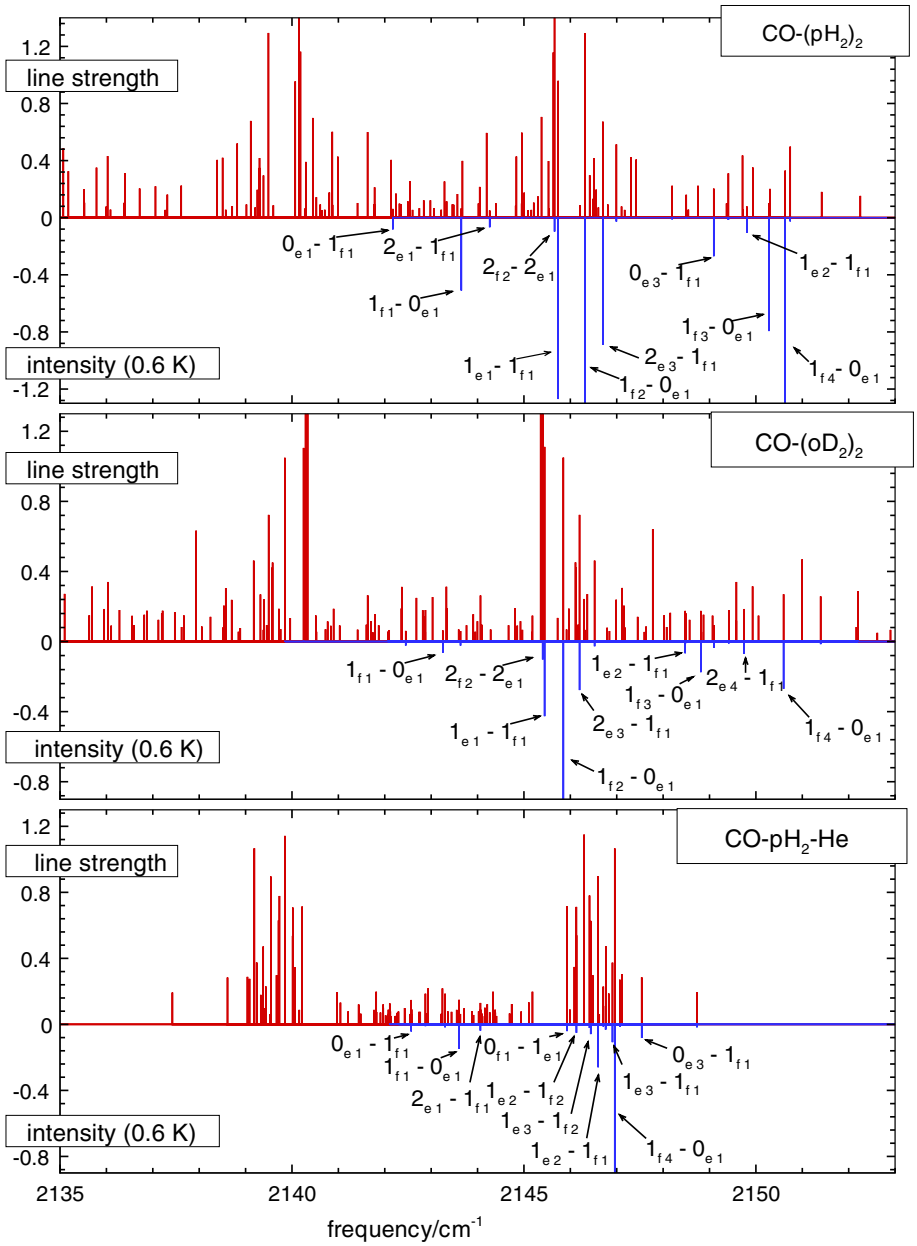

Fig. 6 Calculated infrared spectra of CO–$(pH_2)_2$ (*upper panel*), CO–$(oD_2)_2$ (*middle panel*), and CO–pH_2–He (*lower panel*) for line strength (*upward pointing lines*) and relative intensity at 0.6 K (*downward pointing lines*), respectively. The intensities are expressed relative to (1, f, 2)–(0, e, 1) transition of CO–$(pH_2)_2$ or CO–$(oD_2)_2$, and (1, f, 4)–(0, e, 1) transition of CO–pH_2–He complexes, respectively, whose intensity is equal 1. All the line strength values are multiplied by 10. The relative intensity of CO–$(pH_2)_2$ are also multiplied by 100

one pH_2 and one He (bottom) in the body-fixed frame, as calculated for the ground state of CO–$(pH_2)_2$, CO–$(He)_2$, or CO–pH_2–He using the procedure described in Ref. [27]. It is very useful to develop some intuitive feeling regarding the nature of these species. Iso-surfaces are used to represent the three-dimensional densities, and the z axis is defined to lie on the CO molecular axis. One significant feature of these representations is the fact that the two pH_2 molecules or two He molecules appear to have very different density distributions. It is clear that the density distribution of the first pH_2 or He particle in CO–$(pH_2)_2$ or CO–$(He)_2$ trimer is represented as a at disk and somewhat delocalized in the yz plane, while that of the second pH_2 in CO–$(pH_2)_2$ trimer is highly localized, with two density maxima at regions associated with the pH_2–pH_2 potential minimum. In contrast, the density distribution of the second helium atom in CO–$(He)_2$ trimer (middle panel) is highly delocalized relative to the first, being distributed on an incomplete ring wrapped around the CO molecule. For CO–pH_2–He trimer, the density for pH_2 as particle-1 is located in the *yz* plane as reference, while the density for He as particle-2 is relative to pH_2. As shown in the lowest panel of Fig. 7, the more localized He distribution in CO–pH_2–He than in CO–$(He)_2$ is related to the stronger interaction (deeper well) between the pH_2–He interaction than the He–He one. For all three cases, the density for particle-2 is excluded from the region near particle-1 by the short-range repulsive wall of the pH_2–pH_2, He–He, or pH_2–He potential.

Table 6 Predicted infrared transition frequencies (cm^{-1}), line strengths, and relative intensities at temperature of 0.6 K for CO–$(oD_2)_2$ complex from vibrationally averaged five-dimensional V_{MLRQ} PES

Transitions		Line	Intensity
Upper–lower	Calc.	Strength	(0.6 K)
(1, f, 2)–(0, e, 1)	2,145.849	1.050	1.000
(1, e, 1)–(1, f, 1)	2,145.445	1.111	0.406
(2, e, 3)–(1, f, 1)	2,146.199	0.723	0.264
(1, f, 4)–(0, e, 1)	2,150.597	0.270	0.257
(1, f, 3)–(0, e, 1)	2,148.813	0.175	0.167
(2, f, 2)–(2, e, 1)	2,145.404	1.726	0.097
(1, e, 3)–(1, f, 1)	2,154.309	0.241	0.088
(0,e, 2)–(1, f, 1)	2,149.747	0.186	0.068
(1, e, 2)–(1, f, 1)	2,148.475	0.175	0.064
(1, f, 1)–(0, e, 1)	2,143.251	0.064	0.061
(2, e, 4)–(1, f, 1)	2,149.096	0.093	0.034
(3, f, 3)–(2, e, 1)	2,146.523	0.462	0.026
(0, e, 1)–(1, f, 1)	2,142.452	0.061	0.022
(2, e, 1)–(1, f, 1)	2,143.633	0.060	0.022
(2, f, 4)–(2, e, 1)	2,151.396	0.258	0.014
(1, f, 4)–(2, e, 1)	2,149.416	0.179	0.010
(2, f, 3)–(2, e, 1)	2,148.495	0.160	0.009
(3, f, 4)–(2, e, 1)	2,147.451	0.141	0.008
(3, e, 2)–(3, f, 1)	2,145.361	1.616	0.006
(1, f, 2)–(2, e, 1)	2,144.668	0.093	0.005
(1, f, 3)–(2, e, 1)	2,147.632	0.086	0.005
(1, f, 1)–(2, e, 1)	2,142.070	0.057	0.003
(3, f, 4)–(2, e, 2)	2,146.111	0.452	0.001
(3, e, 3)–(2, f, 1)	2,146.119	0.423	0.001
(1, f, 1)–(1, e, 1)	2,140.250	1.105	0.001
(0, e, 1)–(1, f, 2)	2,139.846	1.049	0.001
(1, f, 2)–(2, e, 2)	2,143.328	0.313	0.001
(1, e, 3)–(2, f, 1)	2,152.200	0.287	0.001
(1, e, 2)–(2, f, 1)	2,146.366	0.271	0.001
(2, f, 2)–(2, e, 2)	2,144.063	0.263	0.001
(2, e, 4)–(2, f, 1)	2,146.988	0.239	0.001
(1, f, 3)–(2, e, 2)	2,146.292	0.243	0.001

The lower and upper states involved in the transitions are numbered with the set of parameters (J, P, $n_{J,P}$). The line strength values are multiplied by 10

Table 7 Predicted infrared transition frequencies (cm^{-1}), line strengths, and relative intensities at temperature of 0.6 K for CO–pH_2–He complex from vibrationally averaged five-dimensional V_{MLRQ} PES

Transitions		Line	Intensity
Upper–lower	Calc.	Strength	(0.6 K)
(1, f, 4)–(0, e, 1)	2,146.958[a]	1.066	1.000
(1, e, 2)–(1, f, 1)	2,146.599	0.898	0.244
(1, f, 1)–(0, e, 1)	2,143.601	0.149	0.140
(1, e, 3)–(1, f, 1)	2,146.908	0.374	0.102
(0, e, 3)–(1, f, 1)	2,147.539	0.285	0.077
(1, e, 3)–(1, f, 2)	2,146.440	0.627	0.055
(1, e, 2)–(1, f, 2)	2,146.131	0.540	0.048
(0, e, 1)–(1, f, 1)	2,142.569	0.148	0.040
(0, f, 1)–(1, e, 1)	2,145.929	0.715	0.038
(2, e, 1)–(1, f, 1)	2,144.061	0.130	0.035
(2, e, 4)–(1, f, 1)	2,146.761	0.112	0.030
(2, f, 3)–(2, e, 1)	2,146.413	0.781	0.020
(0, e, 4)–(1, f, 2)	2,148.729	0.194	0.017
(1, e, 1)–(1, f, 2)	2,143.299	0.186	0.016
(2, f, 4)–(1, e, 1)	2,147.067	0.271	0.014
(2, f, 4)–(2, e, 1)	2,146.770	0.474	0.012
(2, f, 3)–(1, e, 1)	2,146.710	0.229	0.012
(1, f, 2)–(1, e, 1)	2,142.876	0.186	0.010
(2, f, 3)–(2, e, 2)	2,146.129	0.712	0.009
(3, f, 4)–(2, e, 1)	2,147.113	0.303	0.008
(2, e, 2)–(1, f, 2)	2,143.881	0.079	0.007
(2, f, 1)–(1, e, 1)	2,144.209	0.122	0.006
(2, e, 1)–(1, f, 2)	2,143.593	0.060	0.005
(2, f, 4)–(2, e, 2)	2,146.486	0.297	0.004
(1, f, 1)–(2, e, 1)	2,142.108	0.127	0.003
(0, f, 3)–(1, e, 1)	2,153.142	0.062	0.003
(3, f, 4)–(2, e, 2)	2,146.829	0.187	0.002
(3, f, 1)–(2, e, 1)	2,144.382	0.072	0.002
(3, f, 2)–(2, e, 1)	2,144.691	0.066	0.002
(1, f, 2)–(2, e, 1)	2,142.579	0.060	0.002
(2, f, 1)–(2, e, 1)	2,143.912	0.057	0.001
(3, e, 3)–(3, f, 1)	2,146.297	1.150	0.001
(1, f, 2)–(2, e, 2)	2,142.295	0.078	0.001
(3, e, 3)–(2, f, 1)	2,146.770	0.268	0.001
(3, f, 1)–(2, e, 2)	2,144.098	0.065	0.001
(2, f, 1)–(2, e, 2)	2,143.628	0.063	0.001
(3, f, 2)–(2, e, 2)	2,144.407	0.051	0.001

The lower and upper states involved in the transitions are numbered with the set of parameters (J, P, $n_{J,P}$). The line strength values are multiplied by 10

[a] The observed value is 2,146.93 cm^{-1}

Figure 8 shows the "Solvent" pH_2(upper panels), He (middle panels), and pH_2–He (lower panels) densities in the first three torsional levels of CO–$(pH_2)_2$, CO–$(He)_2$, and CO–pH_2–He, respectively. For the $\upsilon_t = 0$ ground states, the density distribution patterns of particle-2 across three complexes are quite different, while for $\upsilon_t = 1$, 2, and 3 excited states, the density distribution patterns are similar among the three species, because at these levels energy patterns are determined by the nodal structures instead of inter-particle interactions and can be explained by a simple one-dimensional particle-in-a-box model along the ϕ coordinate [27, 39].

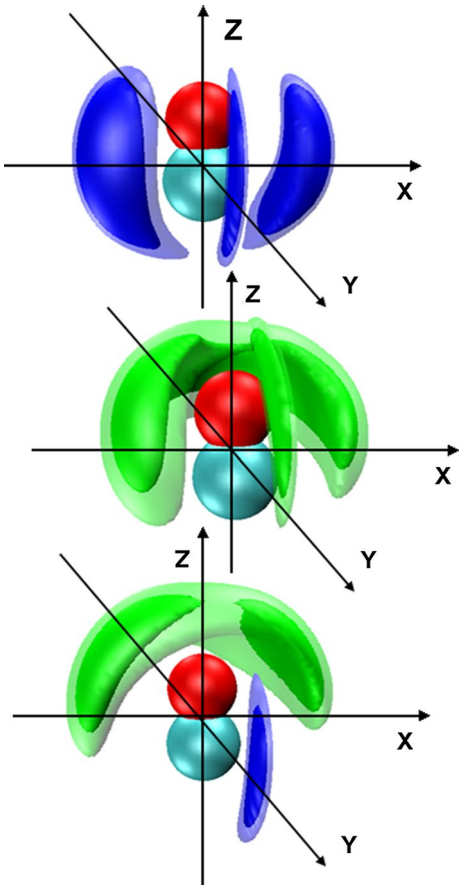

Fig. 7 Three-dimensional representations of the pH_2 density for the ground state CO–$(pH_2)_2$ trimer (*upper panel*) in the body-fixed frame, compared with the helium atom density for a ground-state CO–$(He)_2$ trimer (*middle panel*) and the pH_2–He density of a ground-state CO–pH_2–He trimer (*lower panel*). The position of the first pH_2 or He defines the location of the *yz* plane, while the density of the second pH2 or He particle is shown in the *xy* plane. These results were obtained with the values of the Gaussian standard deviations defining the densities set at $\sigma_x = \sigma_z = 0.25$ Å and $\sigma_y = 0.1$ Å for particle-1 and at $\sigma_x = \sigma_y = \sigma_z = 0.25$ Å for particle-2

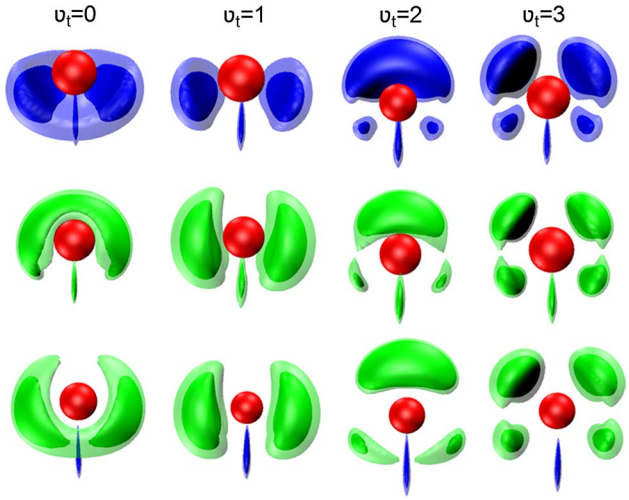

Fig. 8 Three-dimensional representations of the "solvent" (pH_2, He and pH_2–He) density for CO–$(pH_2)_2$ (*upper panels*), CO–$(He)_2$ (*middle panels*), and CO–pH_2–He (*lower panels*) trimers in their four lowest torsion vibrational levels

4 Conclusions

Predicted rovibrational energy levels, microwave, and infrared spectra for CO–$(pH_2)_2$, CO–$(oD_2)_2$, and CO–pH_2–He complexes have been obtained from the vibrationally averaged five-dimensional PESs as a sum of accurate CO–pH_2, CO–oD_2, or CO–He and pH_2–pH_2, oD_2–oD_2, or pH_2–He pair potentials. For CO–$(pH_2)_2$ complex, it is remarkable that the predictions are in good agreement with the experimental measurements of the microwave and infrared transitions, showing that the spectrum can be reliably predicted by this additive approach. Small remaining differences between experiment and theory may in part be due to our neglect of three-body contributions to the interaction energy. For CO–$(oD_2)_2$ trimer, the infrared spectrum has been predicted for the first time. For CO–pH_2–He, one observed IR transition tentatively assigned as b-type $R(0)$ was confirmed based on the calculated line position and intensity. Although many of the transitions for those three complexes have not been observed, our predictions will be a good guidance for future experimental research. The calculated band origin shift from vibrationally averaged five-dimensional PESs associated with the fundamental transition of CO is -0.369 cm^{-1} for CO–$(pH_2)_2$, which is also in good agreement with the experimental value of -0.355 cm^{-1}. The band origin shifts for CO–$(oD_2)_2$ and CO–pH_2–He are also predicted for the first time. In any case, the result indicates that a reduced-dimension treatment of pH_2 or oD_2 rotation based on a "adiabatic-hindered-rotor" average over its relative orientations can yield accurate spectra predictions. Three-dimensional representation of the pH_2, oD_2, or He density in the body-fixed frame is very useful to develop some intuitive feeling regarding the nature of these species, and it clearly shows the density distribution of the second pH_2, oD_2, or He relative to the first one. The pH_2 and oD_2 distributions in the vibrational ground state of CO–$(pH_2)_2$ and CO–$(oD_2)_2$ are highly localized, with two maxima, while the He distribution in CO–$(He)_2$ or CO–pH_2–He is delocalized, with one maximum lying in an incomplete ring wrapped around the CO molecule axis at the O end.

Acknowledgments The authors thank Professor Piotr Jankowski (Nicolaus Copernicus University) for providing us with his V_{12} potential for the H_2–CO complex. This research has been supported by the National Natural Science Foundation of China (Grant Nos. 21003058 and 21273094), the Program for New Century Excellent Talents in University, and the Natural Sciences and Engineering Research

Council of Canada (NSERC). We acknowledge the High Performance Computing Center (HPCC) of Jilin University for supercomputer time.

References

1. Grebenev S, Toennies JP, Vilesov AF (1998) Science 279:2083
2. Nauta K, Miller RE (2001) J Chem Phys 115:10254
3. Tang J, Xu Y, McKellar ARW, Jäger W (2002) Science 297:2030
4. Lehnig R, Jäger W (2006) Chem Phys Lett 424:146
5. Tang J, McKellar ARW (2003) J Chem Phys 119:754
6. Surin LA, Potapov AV, Dumesh BS, Schlemmer S, Xu Y, Raston PL, Jäger W (2008) Phys Rev Lett 101:233401
7. Tang J, McKellar ARW (2004) J Chem Phys 121:181
8. Tang J, McKellar ARW, Mezzacapo F, Moroni S (2004) Phys Rev Lett 92:145503
9. McKellar ARW (2008) J Chem Phys 128:044308
10. Xu Y, Jäger W (2003) J Chem Phys 119:5457
11. McKellar ARW, Xu Y, Jäger W (2006) Phys Rev Lett 97:183401
12. Tang J, McKellar ARW (2003) J Chem Phys 119:5467
13. McKellar ARW, Xu Y, Jäger W (2007) J Phys Chem A 111:7329
14. Li H, Ma YT (2012) J Chem Phys 137:234310
15. Wang L, Xie DQ, Le Roy RJ, Roy P-N (2012) J Chem Phys 137:104311
16. McKellar ARW (2007) J Chem Phys 127:044315
17. Knaap CJ, Xu Y, Jäger W (2011) Mol Spectrosc 268:130
18. Xu Y, Blinov N, Jäger W, Roy P-N (2006) J Chem Phys 124:081101
19. Toennies JP (2013) Mol Phys 111:1879
20. Zeng T, Roy P-N (2014) Rep Prog Phys 77:046601
21. Grebenev S, Sartakov B, Toennies JP, Vilesov AF (2000) Science 289:1532
22. Moroni S, Botti M, De Palo S, McKellar ARW (2005) J Chem Phys 122:094314
23. Tang J, McKellar ARW (2004) J Chem Phys 121:3087
24. Tang J, McKellar ARW (2005) J Chem Phys 123:114314
25. Michaud J, Xu Y, Jäger W (2008) J Chem Phys 129:144311
26. Li H, Le Roy RJ, Roy P-N, McKellar ARW (2010) Phys Rev Lett 105:133401
27. Li H, McKellar ARW, Le Roy RJ, Roy P-N (2011) J Phys Chem A 115:7327
28. Li H, Roy P-N, Le Roy RJ (2010) J Chem Phys 132:214309
29. Zeng T, Guillon G, Cantin JT, Roy P-N (2013) J Phys Chem Lett 4:239
30. Wang L, Xie DQ, Le Roy RJ, Roy P-N (2013) J Chem Phys 139:034312
31. Raston PL, Jager W, Li H, Le Roy RJ, Roy P-N (2012) Phys Rev Lett 108:253402
32. Jankowski P, McKellar ARW, Szalewicz K (2012) Science 336:1147
33. Jankowski P, Surin LA, Potapov A, Schlemmer S, McKellar ARW, Szalewicz K (2013) J Chem Phys 138:084307
34. Li H, Zhang XL, Le Roy RJ, Roy P-N (2013) J Chem Phys 139:164315
35. McKellar ARW (1998) J Chem Phys 108:1811
36. McKellar ARW, Xu Y, Jäger W, Bissonnette C (1999) J Chem Phys 110,10766
37. Surin LA, Roth DA, Pak I, Dumesh BS, Lewen F, Winnewisser G (2000) J Chem Phys 112:4064
38. Wang XG, Carrington T Jr, McKellar ARW (2009) J Phys Chem A 113:13331
39. Wang XG, Carrington T Jr, Tang J, McKellar ARW (2005) J Chem Phys 123:34301
40. Wang XG, Carrington T Jr (2010) Can J Phys 88:779
41. Tang J, McKellar ARW, Wang XG, Carrington T Jr (2009) Can J Phys 87:417
42. Li H, Liu YD, Jäger W, Le Roy RJ, Roy P-N (2010) Can J Phys 88:1146
43. Li H, Roy P-N, Le Roy RJ (2010) J Chem Phys 133:104305
44. Telle H, Telle U (1981) J Mol Spectrosc 85:248
45. Patkowski K, Cencek W, Jankowski P, Szalewicz K, Mehl JB, Garberoglio G, Harvey AH (2008) J Chem Phys 129:094304
46. Chuaqui CE, Le Roy RJ, McKellar ARW (1994) J Chem Phys 101:39
47. Jeziorska M, Cencek W, Patkowski K, Jeziorski B, Szalewicz K (2007) J Chem Phys 127:124303
48. Bramley MJ, Tromp JW, Carrington T Jr, Corey GC (1994) J Chem Phys 100:6175
49. Mladeovic M (2000) J Chem Phys 112:1070
50. Gatti F, Lung C, Menou M, Justum Y, Nauts A, Chapuisat X (1998) J Chem Phys 108:8804
51. Yu HG (2002) Chem Phys Lett 365:189
52. Light JC, Hamilton IP, Lill JV (1985) J Chem Phys 82:1400
53. Chen R, Guo H (2001) J Chem Phys 114:1467
54. Wang XG, Carrington T Jr (2001) J Chem Phys 114:1473
55. Bishop DM, Cheung LM (1980) J Chem Phys 72:5125
56. Parker GA, Snow RL, Pack RT (1976) J Chem Phys 64:1668
57. Peterson KA, McBane GC (2005) J Chem Phys 123:084314
58. McKellar ARW (1991) Chem Phys Lett 186:58